Bulletin of the Seismological Society of America, Vol. 96, No. 4B, pp. S129–S142, September 2006, doi: 10.1785/0120050812

Rupture Propagation of the 2004 Parkfield, California, Earthquake from Observations at the UPSAR

by Jon B. Fletcher, Paul Spudich, and Lawrence M. Baker

Abstract Using a short-baseline seismic array (U.S. Geological Survey Parkfield Dense Seismograph Array [UPSAR]) about 12 km west of the rupture initiation of the 28 September 2004 **M** 6.0 Parkfield, California, earthquake, we have observed the movement of the rupture front of this earthquake on the San Andreas fault. The sources of high-frequency arrivals at UPSAR, which we use to identify the rupture front, are mapped onto the San Andreas fault using their apparent velocity and back azimuth. Measurements of apparent velocity and back azimuth are calibrated using aftershocks, which have a compact source and known location. Aftershock back azimuths show considerable lateral refraction, consistent with a high-velocity ridge on the southwest side of the fault. We infer that the initial mainshock rupture velocity was approximately the Rayleigh speed (with respect to slower side of the fault), and the rupture then slowed to about 0.66β near the town of Parkfield after 2 sec. The last well-correlated pulse, 4 sec after *S,* is the largest at UPSAR, and its source is near the region of large accelerations recorded by strong-motion accelerographs and close to northern extent of continuous surface fractures on the southwest fracture zone. Coincidence of sources with preshock and aftershock distributions suggests fault material properties control rupture behavior. High-frequency sources approximately correlate with the edges of asperities identified as regions of high slip derived from inversion of strong-motion waveforms.

Introduction

Earthquakes are often modeled as expanding surfaces across which relative slip occurs. The edge of the surface expands as a rupture front, and much of the physics of a seismic source centers on its dynamics. Slip initiates when the friction at the rupture front drops from static to dynamic levels. Consequently, seismic radiation is triggered after the passing of the front and can be used to study its behavior. Rupture propagation is usually not directly observed but rather is inferred from simulations of observed ground motions using kinematic slip models. To get around this problem, short baseline arrays (Ishii *et al.*, 2005, Spudich and Cranswick, 1984) have been used as directional antennas to provide direct observation of motion of the rupture front during several earthquakes. The rupture propagation of the **M** 9.0 2004 Sumatra earthquake was recently mapped by stacking seismograms from the 600-seismograph Hi-Net array in Japan (Ishii *et al.*, 2005) and by analyzing three-station arrays of hydrophones in the Indian Ocean (DeGroot-Hedlin, 2005, Tolstoy and Bohnenstiehl, 2005). The source zone of this lethal earthquake extended for over 1300 km (Ammon *et al.*, 2005), and understanding the dynamics of such extended ruptures will be important for assessing the hazard of similar earthquakes. Use of short-baseline arrays may provide an effective tool for rapid determination of earthquake extent or rupture velocity, being more data driven than traditional waveform modeling determinations of rupture kinematics.

UPSAR (U.S. Geological Survey Parkfield Dense Seismograph Array)

In 1988–1989 we installed UPSAR, a 14-station seismic array (Fletcher *et al.*, 1992), 12 km west of Gold Hill (Fig. 1) at the southern end of the section of the San Andreas fault that broke in the 1966 earthquake (Lindh and Boore, 1981) to study the rupture propagation of the anticipated Parkfield mainshock. This section of the fault was characterized as having a high probability of a **M** 6.0 event in the time period 1983–1993 (Bakun and McEvilly, 1984). The anticipated Parkfield earthquake (**M** 6.0) occurred on 28 September 2004 (Langbein *et al.*, 2005).

The location of UPSAR was chosen so that seismic radiation coming from the moving rupture front of a repeat of the 1966 earthquake (see Fig. 1) would subtend a large angle between the ray path from the rupture initiation (north end)

and the ray path from the rupture termination. The array occupied about a 1 km^2 region on the tops of local ridges. The locations of individual stations (Fig. 1, Table 1) were irregularly spaced and were chosen to optimize the central beam width of the array compared to side lobes (Fletcher *et al.*, 1992). Each station consisted of three-component, L-22 velocity transducers from Mark Products (natural frequency of 2 Hz) and three-component, Kinemetrics FBA-23 accelerometers with each channel digitized at 16 bits and 200 samples/sec to be able to describe the complete direction of ground motion and cover its bandwidth of about 30 Hz. Timing was synchronized across the array by phase locking each station's clock to a pulse from a master clock. The main features of this array were its short baseline with respect to

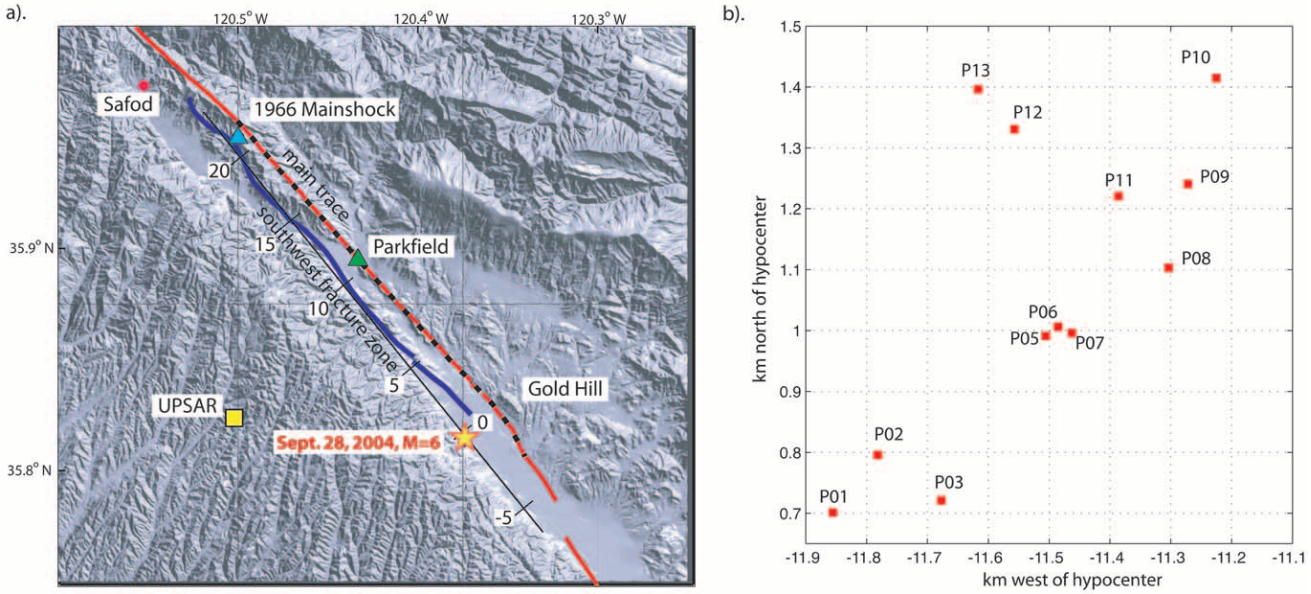

Figure 1. (a) Locations of UPSAR, epicenter of the 28 September 2004 Parkfield earthquake, the southwest fracture zone, the main trace of the San Andreas fault, the town of Parkfield, and the SAFOD drill site. Dashed line shows the fault break of the 1966 **M** 6.0 event (Lindh and Boore, 1981), and the blue triangle is its epicenter. The southwest fracture zone is assumed to be the locus of the 2004 mainshock (star) for at least part of its length based on mainshock and early aftershock locations. The along-strike coordinate axis used in Figures 9 and 10 is shown near the southwest fracture zone. (b) Relative location of the 12 stations, which operated during the earthquake.

Table 1
UPSAR Station Locations, Based on WGS8$_4$

Station	Latitude*	Longitude*	Elevation (m)†	Accuracy (m)*	East Offset (m)†	North Offset (m)†	Elevation Difference (m)†
P01	35 49.272	−120 30.432	576	1.2	−371	−302	−25
P02	35 49.323	−120 30.383	577	1.3	−298	−208	−24
P03	35 49.282	−120 30.313	585	1.5	−192	−284	−16
P04	35 49.338	−120 30.160	583	2.3	38	−180	−18
P05	35 49.428	−120 30.200	597	1.3	−23	−13	−4
P06	35 49.435	−120 30.185	601	1.4	0	0	0
P07	35 49.430	−120 30.170	603	1.3	23	−9	2
P08	35 49.488	−120 30.067	619	3.6	177	98	18
P09	35 49.562	−120 30.043	613	1.2	213	235	12
P10	35 49.657	−120 30.012	604	1.5	260	411	3
P11	35 49.550	−120 30.120	600	1.3	98	213	−1
P12	35 49.612	−120 30.233	585	—	−72	328	−16
P13	35 49.647	−120 30.272	597	1.5	−131	393	−4
P14	35 49.627	−120 30.315	599	1.2	−195	356	−2

*Output from Garmin 76 GPS receiver.
†Offset from P06 determined from latitude and longitude in locally Cartesian frame.

the length of the travel path and its accurate timing, enabling the use of relative differences in arrival time across the array to determine the azimuth of approach and apparent velocity of incident seismic waves.

The locations in Table 1, (referred to here in as "new locations") determined using a GPS unit during removal of the array, supersede the locations given in table 1 of Fletcher *et al.* (1992) (referred to here in as "old locations"). The new locations differ from the old ones because of random measurement errors, a 0.13° error of assumed north in the old locations, and an error of a difference in mean elevation. Mean horizontal offsets between old and new locations, after removing the rotational offsets, are about 2.5 m. Mean vertical offsets are about 2.0 m, after removing a constant elevation difference. All calculations performed in this article used the old locations. Over the 700-m aperture of the array, the 2.5-m horizontal errors are negligible; we believe that the vertical errors are also negligible, as explained subsequently.

Data and Method

Accelerograms from the 28 September 2004 earthquake (Fig. 2) for the fault-parallel component show coherence around the main direct arrivals but are not similar otherwise. Wang *et al.* (2006) discuss the spatial variation of motion in the UPSAR data extensively. Although both north- and east-component accelerations were recorded, the fault-parallel component showed the highest correlation between stations. The *P* wave arrives at 28 sec (time is in sec after 1715 coordinated universal time [UTC] on 28 September 2004) followed about 2 sec later by the hypocentral *S* wave. While the *P* wave is small and emergent on the horizontal components, the *S* wave is more prominent. The largest phase arrives 4 sec after the hypocentral *S* wave. This phase has a maximum amplitude of about 0.3*g*. Although timing is precise across the array, arrivals may suffer site-specific delays caused by differing *S*-wave velocities across the array and by station elevation errors. Consequently, a station-specific time correction was developed as follows. Five aftershocks that were spaced over the length of the rupture zone were used. For each aftershock the relative time delays were measured by cross correlating the S wave at P01 with the *S* wave at all other stations. A plane wave was fit to these arrival times using least squares. A set of residuals was obtained for each event by comparing the expected arrival times for the best-fitting plane wave to the actual arrival times. The expected arrival times of the plane wave included delays or advances caused by variations in station elevation, using a best-fitting surficial *S*-wave speed of 326 m/sec. The direction of the plane wave was not constrained, allowing for possible lateral refraction of the aftershock *S* waves. A set of site delays was obtained by averaging the residuals for all five events. These site delays include the effects of site-to-site variation in *S* velocity and the effects of station elevation errors. For this reason, the effects of elevation errors in the old station locations were nullified by use of the site delays. Use of these site corrections in the correlation analysis increased the values of correlation for the central peaks corresponding to the dominant seismic phases.

We use a moving-window, cross-correlation method to determine the azimuth and apparent velocity ($c_{app} = c/\sin\theta$, where $c = 326$ m/sec is the surface shear-wave velocity and θ is the angle of incidence) of the seismic arrivals starting at the hypocentral *S* wave. This technique transforms acceleration time series from multiple stations into average correlation versus vector slowness ($s = \hat{\mathbf{l}}/c$, where $\hat{\mathbf{l}}$ is a unit direction vector and c is shear-wave velocity) in successive 0.5-sec time windows each advanced by 0.25 sec from the start of the previous window. The window length is based on the approximate duration of the major arrivals in acceleration and the offset by our desire to have closely spaced values in time. Average correlation versus slowness is calculated using the method of Frankel *et al.* (1991), which correlates time series from a pair of stations, one time series lagged according to a given slowness and interstation separation. A final correlation diagram is obtained by averaging the values of correlation for all pairs of stations. Correlation is determined over a grid of slowness values, typically from -0.7 to 0.7, in 0.01 sec/km increments. The time lag for a pair of stations is given by:

$$t_{ij} = s \cdot \mathbf{r}_{ij} + \delta t_i + \delta t_j,$$

where $\mathbf{r}_{ij}$ is the vector pointing from station j to i, δt_i is the site delay determined for station i, $s = (s_E, s_N, s_Z)$ is slowness, s_E and s_N are the slowness component in the east and north directions, respectively, and $s_Z = \sqrt{1/c^2 - s_E^2 - s_N^2}$, where c is the surface shear velocity obtained during the determination of site delays.

Correlation is then calculated by averaging

$$cc_{ij} = \left[\frac{\sum_t x_i(t)\, x_j(t - \tau_{ij})}{\sum_t x_i^2 \sum_t x_j^2} \right]^{1/2} \quad (1)$$

over all pairs of stations i and j, where the sum over t means the sum is over all samples that fall within a specific time window. No tapers were applied to the time windows. x is the ground acceleration time series at a particular station. The azimuth and apparent velocity (c_{app}) corresponding to a given slowness vector are

$$\text{az} = \tan^{-1}\left(\frac{s_E}{s_N}\right), \quad (2)$$

and

$$c_{app} = \frac{1}{(s_E^2 + s_N^2)^{1/2}}. \quad (3)$$

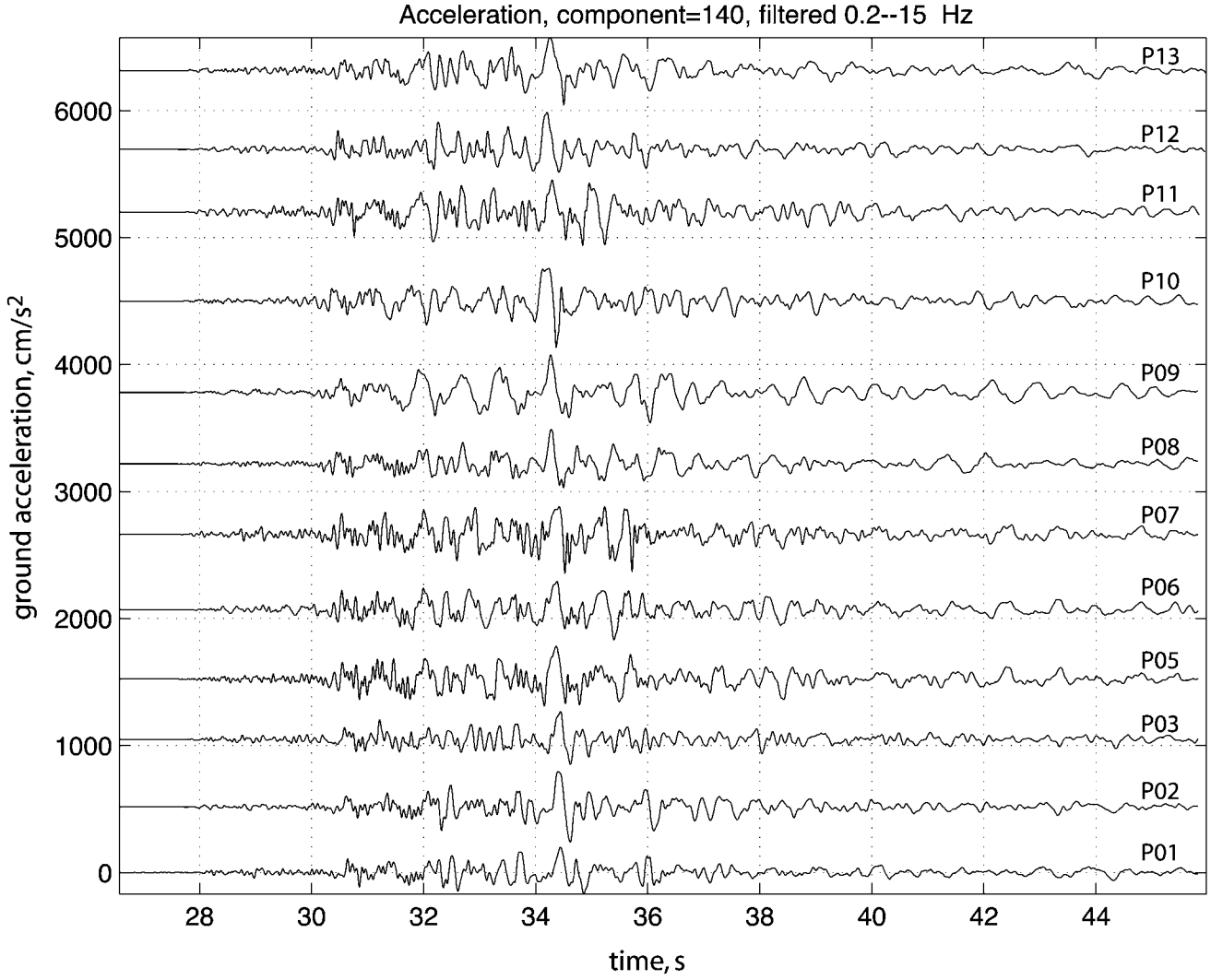

Figure 2. Accelerograms in the fault-parallel (140°) direction, bandpass filtered in the 0.2- to 15-Hz band. Time is seconds after Julian day 272, 17:15, 2004 UTC. The largest peak, 0.3*g*, is the positive pulse at 34.5 sec at P10.

The azimuth is the direction the wave is propagating (measured clockwise from north) and the back azimuth, which points to the energy source, is (az $-$ π). We chose to use the moving-window correlation method because it is a broadband measurement that could be applied successfully to short time windows (e.g., 0.5 sec), giving good temporal resolution of the source. A frequency-domain method, like MUSIC (Goldstein and Archuleta, 1987, Schmidt, 1986), required use of longer time windows and was less satisfactory. We performed a test to determine the level of correlation that would represent a significant arrival. We did this by randomizing the mainshock accelerogram arrival times (by adding a time shift uniformly spread over the interval -0.5 to $+0.5$ sec) and performing the cross-correlation analysis. We found that 98% of the correlation peaks of randomized data had values below 0.4, which we then assume is a threshold value that can be used for testing for significance.

Average correlation functions for the four most significant windows (Fig. 3) are peaked in narrow ranges of slowness for large phases that are well correlated, but show patterns that are more spread out for windows that have no major phase in them (e.g., the correlation for window 31.1–31.6 sec). Values of back azimuth and apparent velocity (equation 3) are given in Figure 4 and Table 2 for the 27 analyzed windows. The accelerogram for P02 (Fig. 4) shows the phases in the time series that are associated with measured azimuth, apparent velocity, or correlation. Peak correlation values are highest for the hypocentral *S* wave at 30 sec, the phase at 32 sec, and the large phase at 34 sec, but drop to 0.4 to 0.5 between these phases. The last possibly significant *S* pulse from the source arrives in the 35.5- to 36.0-sec window. No significant pulses were found in the coda after that phase. We interpret the well-focused high-correlation peaks to represent energy from a spatially com-

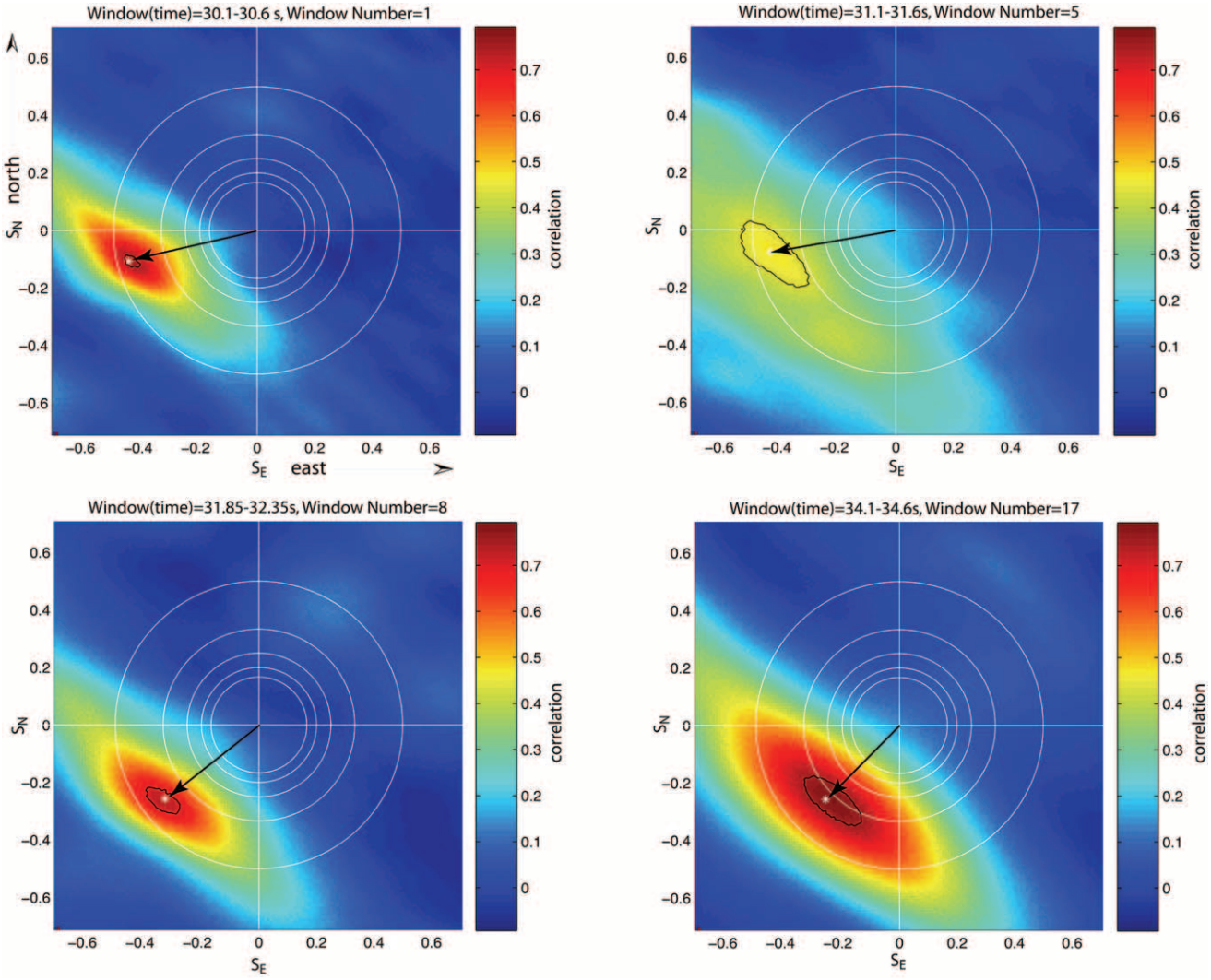

Figure 3. Average correlation as a function of slowness for four windows in the *S*-wave train. Each correlation diagram is for 0.5-sec long window; windows, identified by number, are shown for P02 in Figure 4. The circles denote constant values of apparent velocity of 2, 3, 4, 5, and 6 km/sec from outer to inner circle. The asterisk denotes the peak and the black loop shows the 95% confidence region of the true slowness. S_E and S_N are slowness of the assumed ray in the east and north directions, respectively. Arrows show direction to peak of correlation and consequently the direction of wave propagation.

pact source, whereas peaks with lower values of correlation (above 0.4, but below 0.7–0.8) to be energy coming from larger sections of fault radiating at lower amplitudes.

Rupture propagation can be seen in the change of the back azimuth, which changes from about 77° to 51° in about 1.5 sec and then falls further to 45° at 4 sec after the hypocentral *S* wave. There is a total change in back azimuth of about 32° over a duration of 4 sec. Apparent velocity changes from values near 2.1 km/sec to about 2.8 km/sec at 4 sec after the *S* wave.

Correlation peaks in Figure 3 show black loops that are 95% confidence bounds on the true peak location. We determined these error bounds as follows. We asked, given a common noise-free signal with known slowness at all array elements, if we add random noise to the signal, how far does the resulting peak in average correlation fall from the true slowness? We tested this using two methods for each data window in Figure 3, first, by calculating correlation diagrams for 2000 permutations of data seismograms (i.e., random reassignments of all observed time series to different UPSAR stations), and second, by calculating correlation diagrams for an assumed signal (the average of the 12 seismograms for the window) and 2000 realizations of noise consisting of the residual seismograms (i.e., observed seismograms minus the assumed signal) with their Fourier phase randomized. In both methods, before the permutation

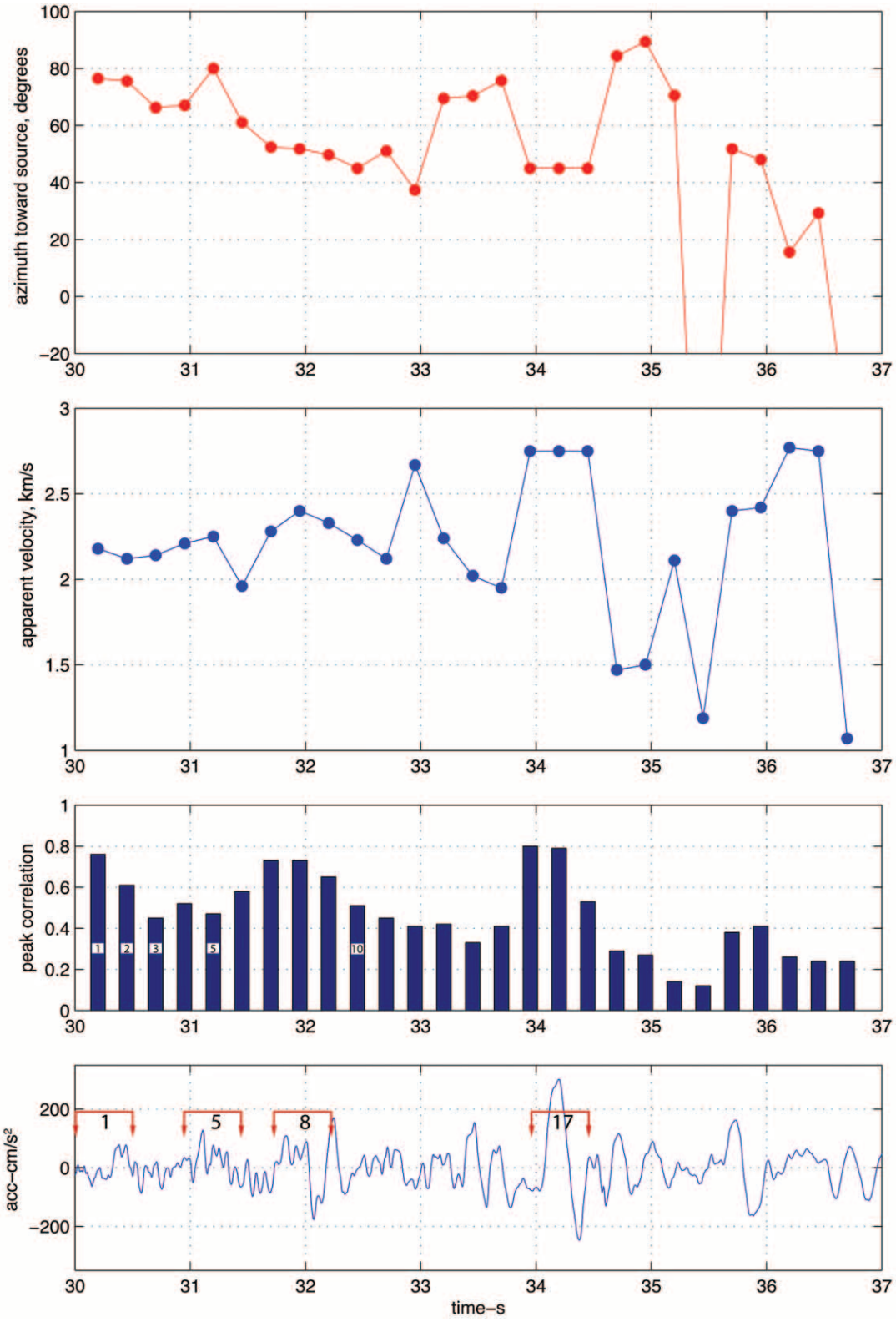

Figure 4. Back azimuth, apparent velocity, average correlation, and 140° component of the P02 ground acceleration versus time for the mainshock starting at the hypocentral *S* wave, which arrives at about 30.3 sec. Three phases have high correlation: the main *S* wave, a phase at 32 sec, and the largest phase on the record at 34 sec. Correlations above 0.4 are significant. Lines bracketed by arrows above the trace of P02 denote 0.5 sec duration-data windows used in computing each of the correlation diagrams in Figure 3. Windows are numbered sequentially (as shown in first few correlation bars), and window start times are offset by 0.25 sec.

Table 2
Rupture Velocities and Correlations

Window Number*	Time†	C_{app}‡	Back Azimuth§	U‖	V#	Rupture Time (sec)	Rupture Velocity**	Correlation
1	30.2	2.18	76.5	−0.4	7.4	0	Inf	0.76
2	30.45	2.12	75.6	0	6.4	0.41	5.42	0.61
3	30.7	2.14	66.3	3.8	7.6	1.07	3.99	0.45
4	30.95	2.21	67	3.4	9	1.1	3.45	0.52
5	31.2	2.25	80	−4.4	7	0.26	16.4	0.47
6	31.45	1.96	61.1	5.6	4.4	2.29	2.29	3.18
7	31.7	2.28	52.4	6.8	8.6	2.15	2.15	3.32
8	31.95	2.4	51.8	6.8	5.08	2.28	3.17	0.73
9	32.2	2.33	49.7	7.6	8.2	2.73	2.91	0.65
10	32.45	2.23	45	9	7	3.14	3.02	0.51
11	32.7	2.12	51	7.6	6.6	3.42	2.4	0.45
12	32.95	2.67	37.4	10.8	10	3.04	3.72	0.41
13	33.2	2.24	69.4	2.8	9.2	3.25	0.99	0.42
14	33.45	2.02	70.3	—	—	—	—	0.33
15	33.7	1.95	75.7	−0.6	4	3.63	1.26	0.41
16	33.95	2.75	45	8.6	11	3.93	2.39	0.8
17	34.2	2.75	45	8.6	11	4.18	2.25	0.79
18	34.45	2.75	45	8.6	11	4.43	2.12	0.53

*Sequential window number (see Fig. 4).
†Time of center of window (see Fig. 4).
‡Apparent velocity in km/sec at UPSAR.
§Back azimuth or azimuth toward source.
‖Along-strike coordinate, (km).
#Depth, (km).
**Average rather than instantaneous (km/sec).

(method 1) or the averaging (method 2) the data were time shifted to cause their correlation peak to lie at zero slowness. Using these procedures we determined the correlation levels (black loops, Fig. 3) above which the true slowness was found 95% of the time. The extrema of these loops were then used to place bounds on the inferred source locations.

Mapping an Observed Back Azimuth and Apparent Velocity onto the Fault

We used the UPSAR records of about 70 aftershocks that occurred on the southwest fracture zone (Fig. 1), which we assume to be the rupture plane of the mainshock, to develop empirical mappings to convert our observations of mainshock back azimuth and apparent velocity to source positions on the fault. We measured aftershock *S*-wave back azimuths and apparent velocities in the same way as for the mainshock. Figure 5 shows the correlation plot for a M 2.5 event and demonstrates the sharply peaked values of correlation above a low background from which values of back azimuth and apparent velocity were obtained for the direct *S* wave. We found that back azimuths of aftershocks do not agree with the straight-line azimuth from UPSAR to their catalog epicenters. Apparently, 3D velocity heterogeneity is refracting the *S*-wave path to the array. Consequently, simply projecting straight rays along the observed back azimuths to source points on the fault would mislocate the sources.

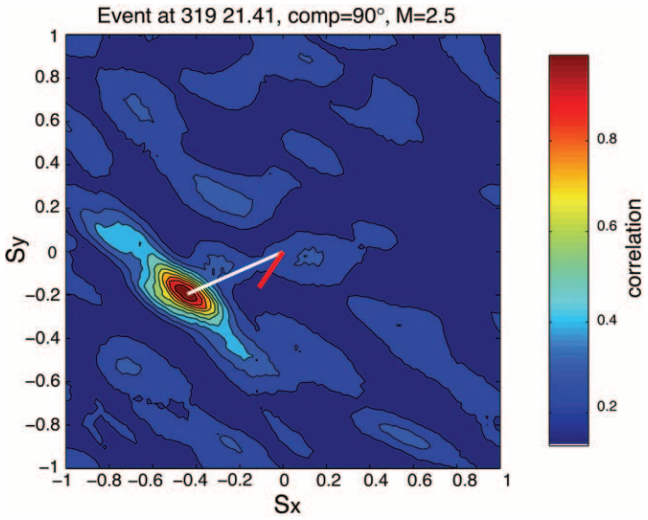

Figure 5. Correlation diagram for the *S* wave of a M 2.5 aftershock on day 319 21:41 UTC, recorded on the east component of acceleration, used in calibrating the back azimuth and apparent velocities. This event had a high peak correlation. Peak is only slightly narrower than width of the mainshock window 8 peak in Figure 3, suggesting spatially compact source for initiation of mainshock rupture.

Because observed aftershock back azimuths depend weakly on source depth whereas observed apparent velocities depend strongly, we used different procedures to develop back azimuth and apparent velocity maps. Almost all events occur in either of two streaks (Hardebeck *et al.*, 2005; Thurber *et al.*, 2006), one at a depth of about 4 km and another at 9 km. We partitioned aftershock back azimuth measurements into two groups, those from the shallow streak (depths between 3 and 7.1 km) and those from the deep streak (8.3–11.2 km). We passed smooth *ad hoc* interpolating functions in a least-squares sense through the back azimuths of these two groups as a function of distance along the strike of the fault (Fig. 6). (Due to scarcity of data, seven aftershocks southeast of the hypocenter are included in both groups.) The black line in Figure 6 shows the straight-line azimuth from UPSAR to the fault, clearly showing that observed back azimuths deviate significantly from straight-line paths. We will comment on this subsequently. The smooth two-dimensional (2D) empirical function in Figure 7 was used to map an observed back azimuth to a locus of possible positions on the fault. Between the depths of 5.05 and 9.75 km, the 2D empirical function was determined by linear interpolation between the blue and red curves in Figure 6. Above or below these depths, the blue and red curves were used, respectively. There is a modest dependence of back azimuth on source depth, which is most apparent at about 7 km in Figures 6 and 7. This means that the lateral refraction of *S* waves is different for deep and shallow sources on this section of the fault.

Because the aftershock apparent velocities depend more strongly on depth, we could not ignore the depth dependence within a streak. Consequently, we passed a smooth 2D interpolant in a least-squares sense through the measured apparent velocities, yielding the empirical function in Figure 8. Because the 3D velocity structure has a significant, somewhat random effect on the apparent velocities, there was no physical basis for choosing the interpolating function, which was an *ad hoc* mixture of polynomials and trigonometric

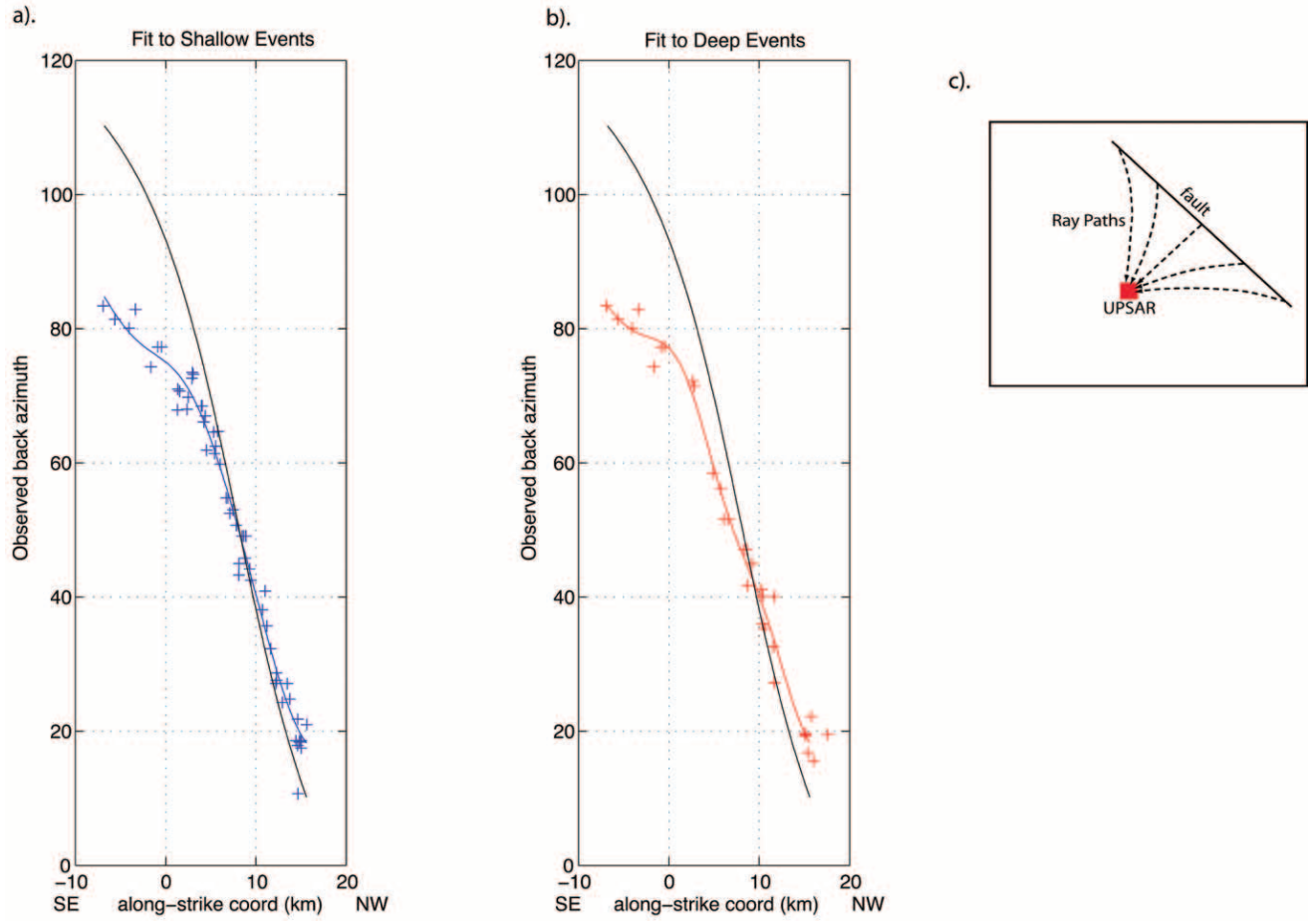

Figure 6. Plot of aftershock back azimuths (crosses) as a function of along-strike position of the aftershock epicenter for streaks of (a) shallow and (b) deep events. Also shown are the smooth curves used to interpolate the back azimuth data (red and blue). The black solid line shows the expected back azimuth if there was no lateral refraction. (c) Cartoon of bending of rays from sources on the San Andreas Fault to UPSAR consistent with our observations.

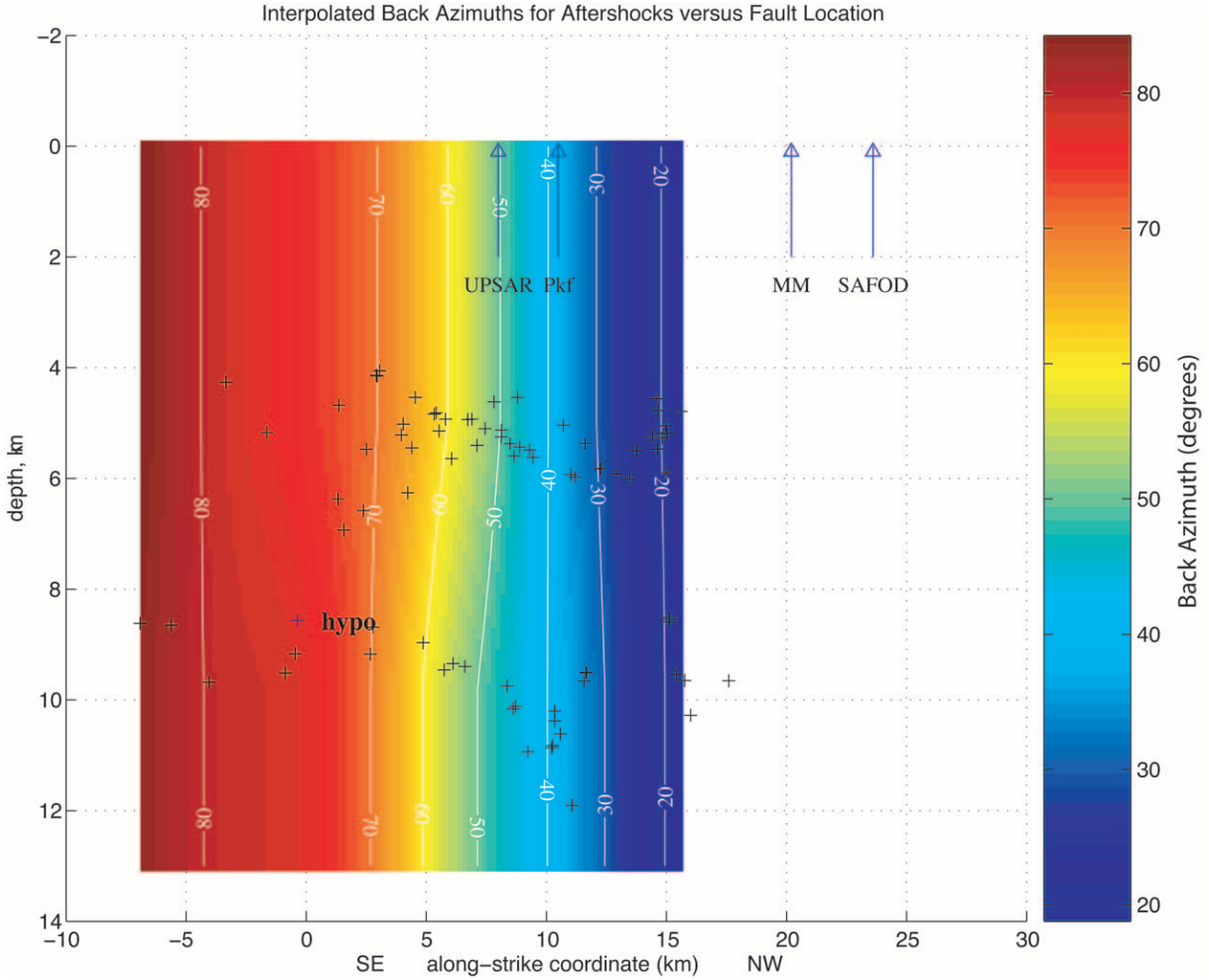

Figure 7. Contours and colors show the fitted interpolating function used to map an observed back azimuth to a position along the strike of the assumed fault plane. Crosses are locations of aftershocks whose back azimuths were fitted. MM is the approximate location of Middle Mountain with respect to the along-strike coordinate. This function and the apparent velocity function in Figure 8 are used together to locate sources on the fault. Although the interpolating function is mostly a function of horizontal position, note the depth dependence at about +7 km.

functions in depth and distance along strike. Finally, source positions are obtained by finding the locations best fitting both the back azimuth and apparent velocity data.

Results

One of the interesting observations we have made is that the lateral refraction shown by the deviations of the red and blue curves from the black curves in Figure 6 implies a pattern of ray bending shown in Figure 6c, which might be related to a high-velocity ridge parallel to the fault. Rays are bent toward the perpendicular from the San Andreas fault to UPSAR. The observed bending is surprising in that it is exactly the opposite of what would be expected from a low-velocity zone in the fault. This bending is qualitatively consistent with 3D velocity models of this region (Eberhardt-Phillips and Michael, 1993; Thurber *et al.*, 2004), which show a strong velocity (*P*-wave) contrast across this part of the fault. The southwest side, which is the Salinian block, is typically faster than the northeast side by about 5%–20% over a 4-km width and contains a ridge of high-velocity material close to the southwest side of the fault, which may be responsible for the observed bending. Azimuths shown in Figure 4 have not been corrected for this effect.

Before presenting the mainshock results we discuss the effects that might be caused by the application of a technique that seeks the best-fitting plane wave in the radiation from a spatially and temporally extended source. We can examine the differences that we might expect between an extended source slip model and the locations of sources from array analysis of records from that extended model. In fact, Spudich and Oppenheimer (1986) did a similar array analysis on synthetic seismograms calculated for a hypothetical Park-

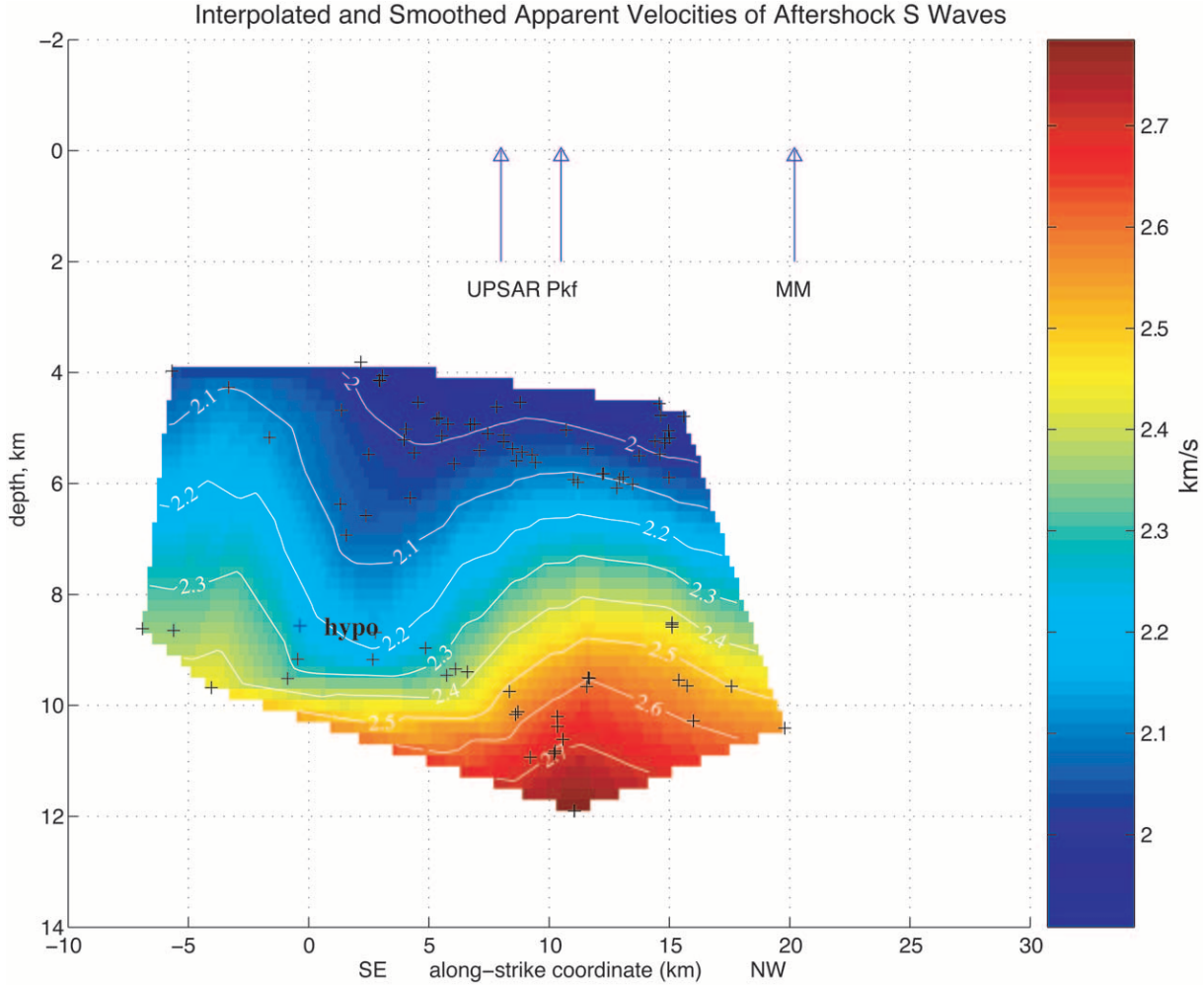

Figure 8. Contours and colors show the fitted interpolating function used to map an observed apparent velocity to a position on the assumed fault plane. Crosses are locations of aftershocks whose apparent velocities were fitted. This 2D function was used with the function in Figure 7 to find the source location on the fault corresponding to any value of measured apparent velocity and back azimuth at the array.

field earthquake. They used a different method (Capon, 1969) and array geometry than used in analyzing the records from the 2004 Parkfield earthquake, but these differences are probably immaterial for this discussion. Their figure 9 shows that the source rupture inferred from the array analysis tends to lag slightly behind the expected source location, possibly because of the averaging of a long arcuate rupture front (actually, an isochone of rupture is imaged in their work). Assuming the same phenomenon might occur in our work, the actual rupture front position may lie ahead (typically northwest) of our inferred source position. However, it is not clear that the same phenomenon will occur in the real data. Their source had uniform slip between about 3- and 12-km depth, whereas slip in the real earthquake may have been concentrated in a narrower depth zone (Liu *et al.*, 2006), so that the source is approximately (within our resolution) a line source, and no effects of arcuate rupture might occur.

Spudich and Oppenheimer (1986) pointed out that the source image obtained by array analysis is not a slip map, because the seismograms observed at the array location are modulated by radiation patterns and local directivity (e.g., their figure 5.) That figure shows that the fault-parallel component is the least likely to be affected by variations of radiation pattern on the fault, which probably accounts for our observation that we get the best results from the fault-parallel component analysis. However, their figure 5 also shows that UPSAR is falling on a node for the fault-parallel component of *S*-wave radiation for sources that are near Middle Mountain (at about 20 km along-strike coordinate). However, sources immediately to the north of the town of Parkfield are not nodal and should be discernable by the array.

Mainshock source locations inferred for each window are shown on the fault plane in Figure 9. Sources are plotted only for windows having average correlation above 0.4, the significance level determined earlier. Green lines show the

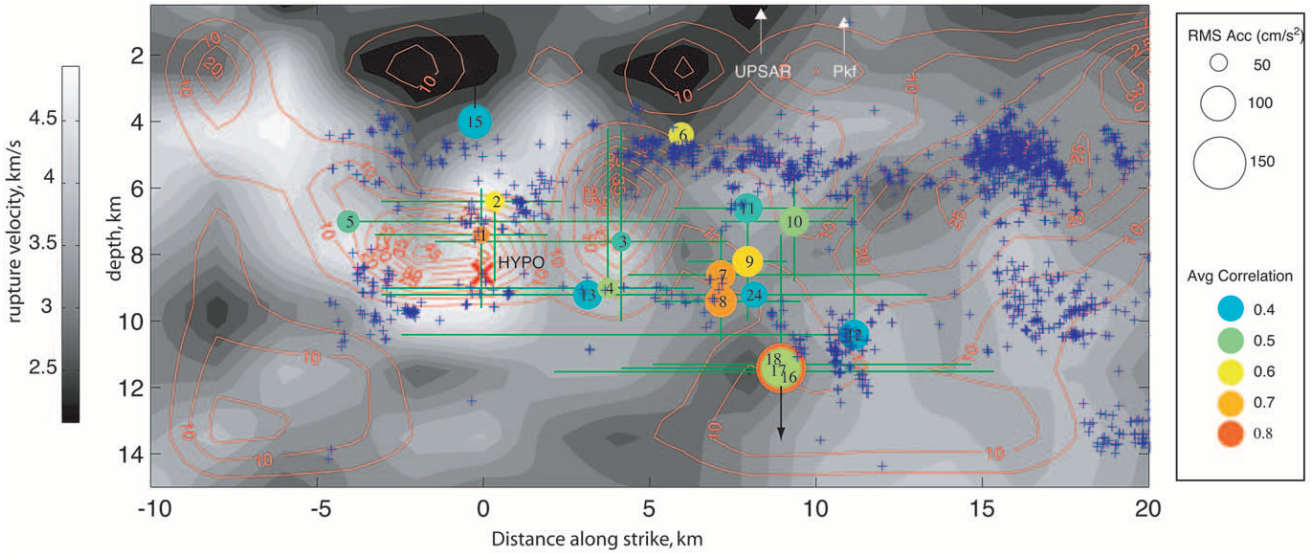

Figure 9. Inferred source locations (colored circles) on a vertical plane approximating the southwest fracture zone of the San Andreas fault. Circle radius is proportional to rms acceleration in the data window. Circle color depends on average correlation. Numbers are window numbers in Figure 4. Green lines show the extent of the 95% confidence limits (Fig. 3) mapped onto the fault. 95% confidence limits are not shown when they extend beyond the region where apparent velocity or back azimuth is defined in Figures 7 and 8. Mainshock hypocenter (X) and aftershocks (+) from Thurber *et al.* (2006). White arrows show closest point to UPSAR and to the town of Parkfield. Background is average rupture velocity (grayscale) and slip (red contours in meters) from Liu *et al.* (2006) and Custodio *et al.* (2006). Black arrows on points 16, 17, and 18 indicate that true depth should probably be about 12 km. Black arrow on source 15 indicates true position is an unknown amount shallower than indicated.

95% confidence limits on the source location based on the correlation peak confidence limits (Figure 3), which is probably the major source of uncertainty. The error bars in Figure 9 do not include horizontal uncertainties caused by arcuate rupture fronts or the back azimuth correction, which is probably less than ± 2 km (Fig. 6), and they do not include the vertical uncertainties based on errors in the aftershock apparent velocity interpolating function (Fig. 8), which are difficult to assess. Sources 16–18 are probably located at a depth of 12 km. Their 2.75 km/sec apparent velocity lies slightly outside the zone where apparent velocity is defined in Figure 8; they are plotted at the closest edge of the zone where apparent velocity is defined. Similarly the apparent velocity for source 15 of 1.95 km/sec puts it shallower than the defined zone in Figure 8.

The location of the inferred sources shows propagation from near the hypocenter northward to near the town of Parkfield over about a 4-sec time span. Initially the sources have depths of about 6–9 km, but deepen to 8–12 km at Parkfield. The catalog hypocenter is located within the 95% confidence limits of our inferred location of hypocentral *S* in windows 1 and 2. The depth discrepancy probably indicates the error in our source mapping rather than a difference between strong-motion and weak-motion hypocenters. Source 5 is the only window consistent with southeastward rupture propagation, but its location is very poorly determined both because of the breadth of its correlation peak (Fig. 3) and the small angle between the *S*-ray direction and the fault plane. The source location of window 8, which includes a significant acceleration pulse (32 sec) (Fig. 4), is particularly well resolved owing to its location near the fault point closest to UPSAR. The horizontal positions of sources 16 and 17, corresponding to the largest acceleration pulse at UPSAR, are not as well resolved, but they are probably deeper than source 8 because their apparent velocities are conspicuously larger than for source 8 (Fig. 3).

Source location is plotted versus time in Figure 10 to show rupture progression. The rupture time of each source in Figure 10 is obtained by subtracting its *S* travel time from its arrival time at UPSAR. As there is no 3D *S*-wave velocity model that covers the UPSAR region that we can use to calculate *S* travel times, we modified *P*-wave travel times from the fault to UPSAR calculated in the 3D model of Thurber *et al.* (2006). We measured *S*-wave times for about 18 aftershocks from different sections of the fault and compared them to predicted *P* times from the Thurber *et al.* (2006) model. We found that by multiplying the *P* times by a V_P/V_S ratio of 1.65 and adding a uniform delay of about 0.9 sec provided a close fit to the observed aftershock *S* travel times.

The average rupture velocities from the hypocenter to sources 7 and 8, which generate the pulse at 32 sec in Figure 4, are 3.32 and 3.17 km/sec, respectively, factors of 0.94

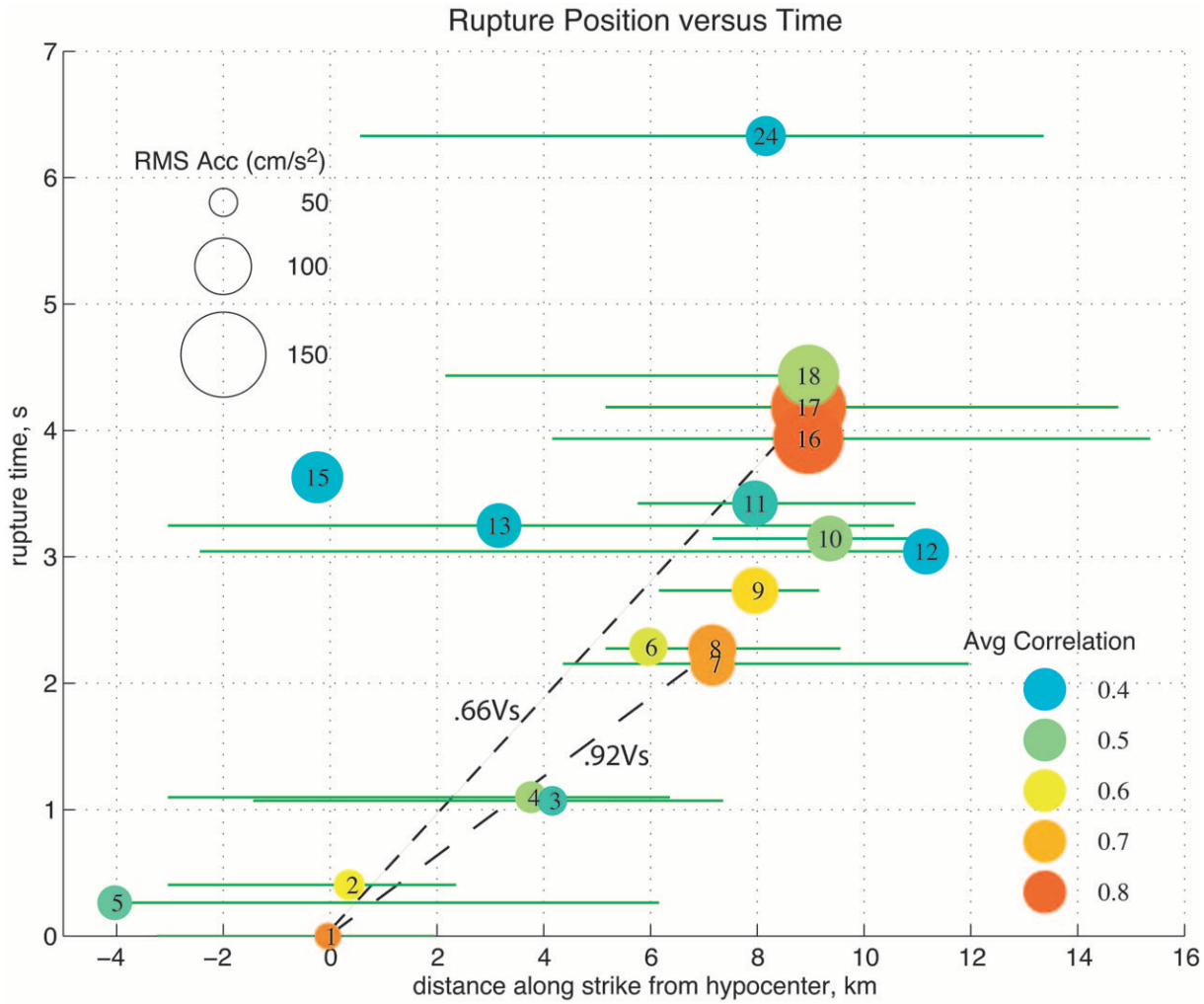

Figure 10. Source locations (colored circles) plotted as distance along strike versus time. Circle color and size as in Figure 9. Dashed lines show the rupture velocity (fraction of shearwave velocity on the northeast, slow, side of the fault) for the main phases shown in Figure 4.

and 0.9 times the *S*-wave velocity (3.52 km/sec) on the northeast side of the fault and 0.88 and 0.84 times V_S (3.78 km/sec) of the southwest side of the fault at 7- to 10-km depth from Thurber *et al.* (2004), who report both *P*-wave and *S*-wave velocities near SAFOD. Average rupture velocity from the hypocenter to the source 17, which generates the largest acceleration at UPSAR (34 sec in Fig. 4) and which might be the source of the large accelerations near the town of Parkfield, is about 2.4 km/sec or 0.68 times the *S*-wave velocity on the northeast side and 0.60 V_S on the southwest side. Figure 10 indicates a very high southeastward rupture velocity to source 5, but given the large error bars on this source's location, we do not believe the apparently high rupture velocity of source 5. An interesting question is whether sources 13, 15, and 24 are the earliest aftershocks of the earthquake, as they are not in the main trend of rupture.

Discussion

Based on the correlation of our sources with preshocks and aftershocks, our results suggest that the rupture behavior of the mainshock was controlled by rheological variations on the fault. The sources of our main pulses (windows 7 and 8, which are well located, and 16 and 17, with somewhat larger error bars) are located very near a deep cluster of aftershocks at about 7–9 km along strike (Fig. 9). Most of the aftershocks, including those in this cluster, locate in the same places as the ambient seismicity before the main event (Hardebeck *et al.*, 2005), despite the fact that the stress distribution on the fault must have changed significantly during the mainshock. This suggests that there are rheological or geometrical variations on the fault plane that persist through the seismic cycle, and the locations of these earthquakes and pulse sources are controlled by the rheological or geometric variations rather than by the preshock stress distribution.

Interestingly, Rymer *et al.* (2006) found cracks along the southwest fracture zone for about 8 km along a segment northwest from the 28 September 2004 epicenter. Cracks were found fairly continuously from a point about 5 km northwest of the hypocenter for a length of about 6 km and then in a second patch 2 km further along the segment. They found cracks on both the San Andreas main trace and the southwest fracture zone, but the slip on the San Andreas is afterslip, compared to coseismic slip on the southwest fracture zone. Also, offsets on newly recognized faults (Rymer *et al.*, 2006) between the main trace and southwest fracture zone are close to where our sources 6–8 and 16–18 are located. Consequently, geologic features also suggest that the point 8–10 km northwest from the hypocenter is a region where the more continuous cracks terminate and where fault complexity links the southwest fracture zone to the main trace.

We do not expect that the picture of rupture that emerges from our study should necessarily agree with the slip distribution inferred from waveform modeling of lower-frequency data. It is possible that acceleration pulses observed at UPSAR are not radiated from slip maxima. High frequencies are radiated from spatial variations of slip and changes in rupture velocity (Madariaga, 1978; Spudich and Frazer, 1984). For example, it is well known that a Haskell model (strip of uniform slip moving down a rectangular fault plane) radiates high frequencies only from its edges, suggesting that pulses recorded in acceleration at UPSAR may come from the edges of the high-slip zones. The isochrone model of rupture (Spudich and Frazer, 1984) predicts high-frequency seismic radiation from acceleration of the rupture front, and the passage of the rupture front through strong gradients of slip. Figure 9, which compares the location of sources of high-frequency radiation with the slip model of Liu *et al.* (2006) and Custodio *et al.* (2006), shows that most of our sources are on the edges of the high-slip regions. Average rupture velocity (rather than instanteous rupture velocity) is also shown, and our sources are in regions where rupture velocity is changing, but it is hard to judge the importance of this correlation because the rupture velocity is hardly ever constant in this model. Our rupture times agree well with those of Liu *et al.* (2006) for sources 1–9 (except 5), but our sources 16–18 are significantly delayed with respect to the rupture time for their location in the Liu *et al.* (2006) model.

The slip model of Liu *et al.* (2006) for the mainshock concentrates slip in the regions devoid of aftershocks between depths of 5 and 10 km (Fig. 9) and extending 20 km northwest from the hypocenter. It might be that acceleration pulse 8 is a rupture deceleration phase radiated when the subshear rupture encountered a change in material properties at the aftershock zone after propagating through a high-slip patch. The largest acceleration pulse, window 17, appears to originate from a source at a deeper extension of the aftershock cluster and might correspond to the delayed rupture of a strong patch on the fault at that location, or it could be caused by rupture acceleration into a high-slip region extending from 10 to 20 km along strike (see red contours updip from 12 km, Fig. 9). It should be noted that the sources of the northernmost (source 17) and southernmost (source 5) acceleration pulses observed at UPSAR agree well with the areas of large ground acceleration recorded at stations of the California Geological Survey in this region (Shakal *et al.*, 2005), suggesting that we have not mislocated them. However, error bars on source 17 extend to at least 15 km along strike (most clearly seen in Fig. 10), so it is possible that this pulse could represent rupture of the high-slip zone 15 km northwest of the hypocenter. It is surprising that we do not observe any pulses coming from the slip maxima northwest of the town of Parkfield (Fig. 9), but this might be caused by the fact that *S* waves from that part of the fault are nodal on the fault-parallel component and the rupture is traveling away from UPSAR. However, we note that we do not see any pulses from that part of the fault on the fault-normal component of motion either, so perhaps there are no strong changes of slip or rupture velocity on that part of the fault to generate acceleration pulses at UPSAR.

The UPSAR data suggest that high-acceleration pulses originate from spatially compact source regions. The largest acceleration pulses in Figure 4 have the highest correlation, meaning that they are better approximated by a plane wave than are the intervening lower accelerations (not shown).

Our rupture velocities are variable and demonstrate the importance of this parameter in studying source physics. The rupture velocity was initially high, near the Rayleigh velocity, and then slowed. This implies that near the hypocenter the fault was near failure (low *S* parameter) (Andrews, 1976), but this condition did not persist over the entire fault. The comparison of this observation with other direct observations of rupture will enhance our understanding of earthquake nucleation and extension.

This work directly locates the source of seismic radiation from a **M** 6.0 earthquake from its initial site to a point about 10 km northwest near the town of Parkfield. Although correlations are strongly peaked for three main phases suggesting that the sources of these phases are compact, the poorly correlated waves observed between these phases are probably caused by radiation from broader sections of fault. Consequently, it seems the fault can be viewed as alternately radiating with high coherence and then incoherence. This raises the question of what fault frictional or geometric properties cause the smallest sections of the fault to radiate the largest pulses. Small arrays offer a new set of observations that can provide insight into these processes. In addition, such arrays provide an effective way of observing rupture propagation (Ishii *et al.*, 2005, Spudich and Cranswick, 1984) in a more direct way than waveform modeling, and thus might provide an additional type of data for near-real-time earthquake monitoring.

Conclusions

High-frequency radiation from the 28 September 2004 earthquake has been mapped to the San Andreas fault using

estimates of back azimuth and apparent velocity determined at UPSAR. Back azimuths show considerable lateral refraction consistent with a high-velocity body on the Southwest side of the fault. Both apparent velocities and back azimuths are corrected to true back azimuths and depths using calibration curves developed from observations of aftershocks. Initial rupture velocities are high near the shear-wave velocity, slowing so that the average 4 sec after initiation is about 0.66β. Correlation is high for about 4 sec (with reference to the initial *S* wave), ending with a large pulse that may originate from a point where the rupture jumped from the southwest fracture zone to the main trace of the San Andreas fault, near the area where high peak accelerations were observed on local strong-motion instruments. After the large pulse at 4 sec after the hypocentral *S*-wave arrival time, the correlation is low, suggesting a marked change in the organization of the rupture front.

Acknowledgments

We are grateful to George Work and family, the owners of the land on which UPSAR was installed, for their patience and cooperation in building the array. We would also are indebted to the many other employees at the USGS who helped with the installation and maintenance of the array, particularly Russell Sell. J. Hardebeck gave us aftershock hypocentral information in advance of publication and calculated travel times in the 3D Parkfield structure. C. Thurber gave us his 3D *S*-velocity structure. We also thank Susana Custodio and Pengshan Liu at University of California Santa Barbara for their slip model. UPSAR time series for the mainshock is available at http://nsmp.wr.usgs.gov/data_sets/20040928_1715.html thanks to Chris Stephens at the USGS.

References

Ammon, C. J., C. Ji, H.-K. Thio, D. Robinson, S. Ni, V. Hjorleifsdottir, H. Kanamori, T. Lay, S. Das, D. Helmberger, G. Ichinose, J. Polet, and D. Wald (2005). Rupture process of the 2004 Sumatra-Andaman earthquake, *Science* **308,** 1133–1139.

Andrews, D. J. (1976). Rupture velocity of plane strain shear cracks, *J. Geophys. Res.* **81,** 5679–5687.

Bakun., W. H., and T. V. McEvilly (1984). Recurrence models and Parkfield, California earthquakes, *J. Geophys. Res.* **89,** 3051–3058.

Capon, J. (1969). High resolution frequency-wavenumber spectral analysis, *Proc. IEEE* **57,** 1408–1418.

Custodio, S., P. Liu, and R. J. Archuleta (2005). 2004 M_w 6.0 Parkfield, California, earthquake: inversion of near-source ground motion using multiple datasets, *Geophys. Res. Lett.* **32,** L23312, doi 10.1029/2005GL024417.

DeGroot-Hedlin, C. D. (2005). Estimation of the rupture length and velocity of the great Sumatra earthquake of Dec. 26, 2004 using hydroacoustic signals, *Geophys. Res. Lett.* **32,** L11303.

Eberhardt-Phillips, D., and A. J. Michael (1993). Three-dimensional velocity structure and seismicity in the Parkfield region, central California, *J. Geophys. Res.* **98,** 15,737–15,758.

Fletcher, J., L. M. Baker, P. Spudich, P. Goldstein, J. D. Sims, and M. Hellweg (1992). The USGS Parkfield, California, dense seismograph array-UPSAR, *Bull. Seism. Soc. Am.* **82,** 1041–1070.

Frankel, A., S. Hough, P. Friberg, and R. Busby (1991). Observations of Loma Prieta aftershocks from a dense array in Sunnyvale, California, *Bull. Seism. Soc. Am.* **81,** 1900–1922.

Goldstein, P., and R. J. Archuleta (1987). Array analysis of seismic signals, *Geophys. Res. Lett.* **14,** 13–16.

Hardebeck, J. L., F. Waldhauser, A. J. Michael, and W. L. Ellsworth (2005). Parkfield earthquake locations: implications for structure and fault mechanics, *Seism. Res. Lett.* **76,** 211.

Ishii, M., P. M. Shearer, H. Houston, and J. E. Vidale (2005). Extent, duration, and speed of the 2004 Sumatra-Andaman earthquake imaged by the Hi-Net array, *Nature* doi 10.1038.

Langbein, J. L., R. Borcherdt, D. Dreger, J. Fletcher, J. L. Hardebeck, M. Hellweg, C. Ji, M. Johnston, J. R. Murray, R. Nadeau, M. J. Rymer, and J. A. Treiman (2005). Preliminary report on the 28 September 2004, M 6.0 Parkfield, California earthquake, *Seism. Res. Lett.* **76,** 10–26.

Lindh, A. G., and D. M. Boore (1981). Control of rupture by fault geometry during the 1966 Parkfield earthquake, *Bull. Seism. Soc. Am.* **71,** 96–1116.

Liu, P., S. Custodio, and R. Archuleta (2006). Kinematic inversion of the 2004 **M** 6.0 Parkfield earthquake including an approximation to site effects, *Bull. Seism. Soc. Am.* **96,** no. 4B, S143–S158.

Madariaga, R. (1978). The dynamic field of Haskell's rectangular dislocation fault model, *Bull. Seism. Soc. Am.* **68,** 869–888.

Rymer, M. J., J. C. Tinsley, J. A. Treiman, J R. Arrowsmith, K. B. Clahan, A. M. Rosinki, W. A. Bryant, H. A. Snyder, G. S. Fuis, N. Toké, and G. W. Baden (2006). *Bull. Seism. Soc. Am.* **96,** no. 4B, S11–S27.

Schmidt, R. O. (1986). Multiple emitter location and signal parameter estimation, *IEEE Trans. Ant. Prop.* **AP-34,** 276–280.

Shakal, A., V. Graizer, M. Huang, R. Borcherdt, H. Haddadi, K.-W. Lin, C. Stephens, and R. Roffers (2005). Preliminary analysis of strong-motion recordings from the 28 September 2004 Parkfield, California earthquake, *Seism. Res. Lett.* **76,** 27–39.

Spudich, P., and E. Cranswick (1984). Direct observation of rupture propagation during the 1979 Imperial Valley earthquake using a short baseline accelerometer array, *Bull. Seism. Soc. Am.* **74,** 2083–2114.

Spudich, P., and L. N. Frazer (1984). Use of ray theory to calculate high-frequency radiation from earthquake sources having spatially variable rupture velocity and stress drop, *Bull. Seism. Soc. Am.* **74,** 2061–2082.

Spudich, P., and D. Oppenheimer (1986). Dense seismograph array observatios of earthquake rupture dynamics, S. Das, J. Boatwright, and C. Scholz (Editors), American Geophysical Monograph 37, 285–296.

Thurber, C., S. Roecker, H. Zhang, S. Baher, and W. Ellsworth (2004). Fine-scale structure of the San Andreas fault zone and location of the SAFOD target earthquakes, *Geophys. Res. Lett.* **31,** doi 10.1029/2003GL019398.

Thurber, C., H. Zhang, F. Waldhauser, J. Hardebeck, A. Michael, and D. Eberhart-Phillips (2006). Three-dimensional compressional wavespeed model, earthquake relocations, and focal mechanisms for the Parkfield, California, region, *Bull. Seism. Soc. Am.* **96,** no. 4B, S38–S49.

Tolstoy, M., and D. R. Bohnenstiehl (2005). Hydroacoustic constraints on the rupture duration, length, and speed of the Sumatra-Andaman earthquake, *Seism. Res. Lett.* **76,** 419–425.

Wang, G-Q., G-Q. Tang, C. R. Jackson, X-Y. Zhou, and Q-L. Lin (2006). Strong ground motions observed at the UPSAR during the 2003 San Simeon (**M** 6.5) and 2004 Parkfield (**M** 6.0), California, earthquakes, *Bull. Seism. Soc. Am.* **96,** no. 4B, S159–S182.

U.S. Geological Survey
345 Middlefield Road
Menlo Park, California 94025

Manuscript received 15 September 2005.